

pubs.acs.org/acsaelm Article

Highly Conductive Copper—Silver Bimodal Paste for Low-Cost Printed Electronics

Amin Zareei, Sarath Gopalakrishnan, Zeynep Mutlu, Zihao He, Samuel Peana, Haiyan Wang, and Rahim Rahimi*



Cite This: ACS Appl. Electron. Mater. 2021, 3, 3352-3364



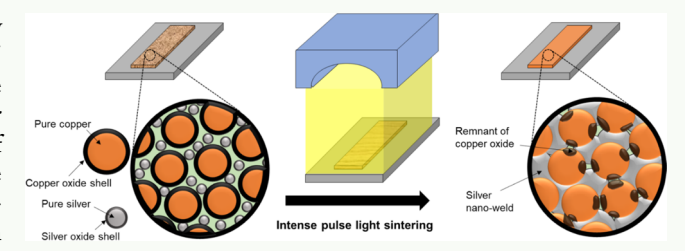
ACCESS

III Metrics & More

Article Recommendations

SI Supporting Information

ABSTRACT: Printed electronics are circuits that are additively manufactured using conductive pastes composed of micro-/nanoconductive metal particles. Silver-based compounds are the most widely used metals for such pastes due to their superior conductivity and oxidation stability. However, the high cost of silver (Ag) has demanded its replacement with more cost-effective and abundant metals such as copper (Cu). Despite its cost-effectiveness and abundance, Cu suffers from high oxidation tendency and sintering temperature that have limited its



widespread utilization in printed electronics. In this work, we have developed a low-cost hybrid bimodal paste composed of Cu microparticles (1–5 μ m) and Ag nanoparticles (20–30 nm) (CuMPs/AgNPs) via nondestructive photonic sintering. The concurrent melting of AgNPs and catalytic reduction of CuMPs allow the paste to be sintered at considerably low temperatures using an intense-pulsed light (IPL) source. The required light energy density for effective sintering of different mixing ratios of AgNPs and CuMPs was systematically measured using electrical, optical, and mechanical characterization techniques. These analyses revealed that a minimum of 16 wt % AgNPs in the bimodal CuMP/AgNP paste with an IPL irradiation energy of 10.6 J/cm² and pulse duration of 5 ms achieved a minimum sheet resistance of 0.072 Ω / that results from localized melting of AgNPs between adjacent CuMPs. Furthermore, the CuMP/AgNP films with a minimum of 6 wt % AgNPs showed significantly improved oxidation stability characteristics even after 7 days of incubation in accelerated oxidation conditions [70 °C and 100% relative humidity (RH)]. As a proof of concept, we demonstrated an application of the developed paste (CuMPs-6 wt % AgNPs) by directly printing a wireless resonant moisture sensor onto the interior region of a cardboard package box, which is capable of performing in situ monitoring of the moisture ranging from 30 to 85% RH with an average linear sensitivity of -3.08 % RH/MHz.

KEYWORDS: printed electronics, CuMP/AgNP bimodal paste, photonic sintering, high oxidation resistance, wireless moisture sensor

■ INTRODUCTION

In recent years, there has been a growing interest in utilizing novel additive manufacturing technologies as a suitable fabrication method that enables high-volume production of various low-cost electronic devices, such as radiofrequency (RF) identification tags, wearable electronics, batteries, and sensors. 1-5 Unlike conventional photolithography based fabrication methods which require several lengthy and timeconsuming processing steps, printed electronics (PE) offer a great number of advantages^{4,6-8} in the manufacturing of electronic devices by providing a more cost-effective and efficient use of materials with minimal waste production.^{3,9,10} In addition, printed technologies are frequently used for the fabrication of conductive elements (e.g., contacts, interconnects, antennas, and electrodes) for flexible electronic devices on a wide range of polymeric substrates that are chemically and thermally incompatible with conventional integrated circuit processes.

In general, the conductive pastes used in such printed elements are created by dispersing small particles of conductive materials (e.g., precious metal particles) into an organic binder (e.g., polyvinyl alcohol, polyvinylpyrrolidone, and polyvinyl butyral) that is dissolved in an organic solvent. After printing the desired pattern, the paste needs to be properly dried or cured to remove the solvent, strengthen the matrix, and form percolation paths of conductive particles. Among different conductive filler particles used in many conductive inks and pastes, silver (Ag) has been reported to be the most widely used material due to its high conductivity ($\sigma = 6.3 \times 10^7 \ \Omega^{-1} \ m^{-1}$) and oxidation resistance against many other metals. Despite the obvious merits of silver-based conductive pastes such as the excellent conductivity and resistance to oxidation, the continuous increase in the raw material prices of precious

Received: April 14, 2021 Accepted: June 11, 2021 Published: August 13, 2021





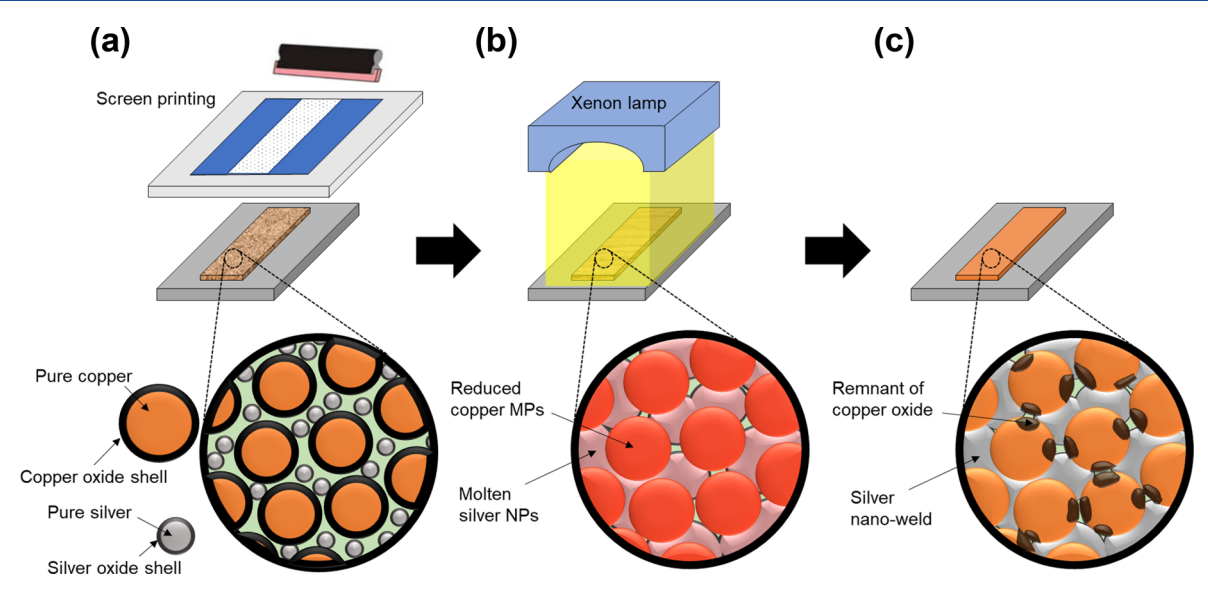


Figure 1. Schematic of the nanowelding process of CuMPs by AgNPs via xenon lamp irradiation, (a) fabrication of CuMP/AgNP hybrid bimodal trace by screen printing, (b) photonic sintering and photothermochemical reduction of the trace by a xenon lamp, and (c) sintered trace with reduced CuMPs welded together by AgNPs.

metals and the need for high temperature for curing/sintering process have restricted their wide use to certain substrates on which they can be printed. Lately, copper (Cu)-based conductive pastes have been increasingly considered as a potential replacement material for expensive noble-metal-based conductive pastes. However, despite its lower cost, it has an inherent tendency to oxidize under ambient conditions due to the relatively low oxidation potential energy of Cu ions (0.34 V) as compared to Ag (0.799 V), which induces the inevitable formation of an oxide layer on the Cu particles with low film electrical conductivity after printing. 16 Therefore, Cu-based pastes will require a critical postdeposition sintering process to transform printed patterns into conductive, solid metal traces. 17 In general, sintering processes of PE can be categorized into chemical- and thermal-based approaches. Most chemical sintering approaches involve exposing the printed traces to a series of chemical solutions that first remove the oxide layer, followed by electroless deposition of Cu between the printed particles, forming a densely packed conductive structure. 18 Although such chemical sintering processes are performed at relatively low temperatures with cost-effective materials, the required long durations of submerging the printed traces in liquid solutions impede its wide industrial use, limiting its application to water-resistant substrates.

In contrast, thermal-based approaches involve the application of heat to decompose and remove the oxide layer and sinter the metal particles within the printed trace. 19 Although it is relatively easy and cheap, the high temperatures (>1000 $^{\circ}$ C) of postprinting processes that are often required to reduce the oxide layer (CuO and Cu₂O) and sinter Cu-based conductive pastes with micron-sized particles have limited their application onto inorganic substrate materials. 4 To reduce the sintering temperature and have better compatibility with temperature-sensitive substrates (e.g., polymer and paper), many research groups have developed new forms of Cu-based conductive pastes by utilizing smaller-sized particles or protecting the Cu-particles with a nonoxidizable shell, generally formed by various polymers and noble metals (Ag). 18 The melting temperature of Cu nanoparticles

decreases with their diameter, enabling the utilization of nondestructive and selective sintering techniques such as laser and photonic sintering that can effectively reduce, melt, and sinter these nanoparticles with significantly lower temperature as compared to larger particles. 16 Although Cu-nanoparticlebased inks²⁰⁻²⁴ have shown to require lower sintering temperature due to nanoparticle melting-point depression phenomenon, 16,25 they tend to have relatively low oxidation resistance even after sintering, resulting in instability and observed decrease in electrical conductivity over time. 26-28 One of the commonly used techniques to minimize Cu nanoparticle oxidation is to use core/shell nanoparticle structure composed of Cu as the core inner material and a noble metal shell as the outer layer.²⁹ In this approach, coating of an oxidation-resistant and highly conductive metal such as Ag onto the surface of the Cu core can both enhance the conductivity and prevent copper oxidation. 18,28 Although this approach has shown to provide a high level of conductivity up to 13.5 $\mu\Omega$ ·cm, it still faces several challenges such as requiring an inert sintering environment, lengthy synthesis process, and high cost of Cu nanoparticles. $^{18,30-32}$ In addition, such inks are based on the suspension of metallic nanoparticles in lowviscosity carrier solutions that often exhibit good levels of electrical conductivity only after multilayer printing and subsequent sintering. Core/shell structures can also be used to develop conductive pastes composed of silver-coated copper microparticle conductive fillers. Despite lower cost and higher oxidation resistance compared to silver-coated copper nanoparticles, such materials face a lengthy, cumbersome, and expensive synthesis process that results in significantly higher final cost of the paste.

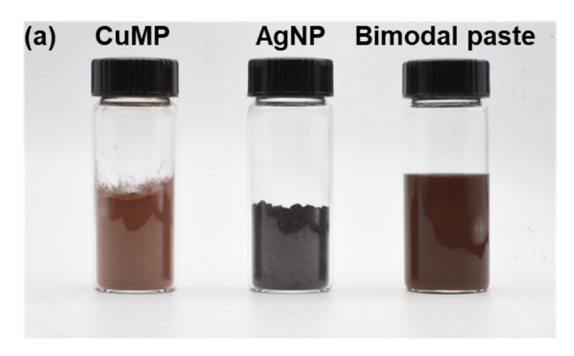
The second category of ink formulation is bimodal hybrid Cu inks which can be divided into two groups of Cu micro- or nanoparticles mixed with another nanomaterial.^{33–41} The addition of the nanomaterial improves the microstructure of the printed trace by filling the pores of the pattern, resulting in improved packing density with less susceptibility to mechanical failure. It also improves the conductivity of the pattern by providing low effective sintering temperature that could be easily achieved by faster sintering methods, such as micro-

waves, IPL, and laser beam. For instance, a mixture of Cu nanoparticle and multiwalled carbon nanotube (MWCNT) ink sintered by photonic sintering has been shown to achieve conductivity of up to 7 times higher than that of bulk copper. This is mostly due to the superior light absorption of the MWCNT; however, the use of the MWCNT can significantly increase the overall price of the ink. In a recent study, Joo et al. showed that by using a mixture of Cu microparticles and nanoparticles and flash light sintering, they were able to achieve 67 and 61% relative improvement in resistivity as compared to only nanoparticle- and microparticle-based Cu pastes, respectively. However, the developed ink still suffered from fast oxidation of Cu nanoparticles both during and after sintering, resulting in unstable electrical conductivity.

Here, we have developed a low-cost hybrid bimodal ink composed of CuMPs and AgNPs to be sintered by capable of sintering by means of rapid IPL sintering. The simultaneous melting of AgNPs and selective catalytic reduction of the outer oxide layer of the CuMPs during the IPL irradiation process enable an effective interconnected structure with reduced contact resistance between the CuMPs. In other words, the low-melting-point AgNPs serve as nanowelders between the CuMPs while also minimizing the surface reoxidation of CuMPs after the photothermochemical reduction process (Figure 1). The use of CuMPs in the paste provides a favorable cost reduction and the ability to print thick conductive metal traces for different printed RF and antenna applications. In this paper, we present the results of a systemic study in identifying the optimum IPL process for effective sintering of screenprintable pastes with different weight percentage ratios of CuMPs and AgNPs. The conductive films are evaluated by electrical, optical, and mechanical characterizations and assessed to find the threshold weight percentage of AgNPs in the paste to attain high electrical conductivity while remaining economically viable for the production of low-cost printed wireless sensors. As a proof-of-concept, we demonstrate the use of the developed paste with optimal bimodal CuMP to AgNP ratio and IPL sintering process for printing a wireless passive moisture sensor that could monitor the humidity level within a sealed package.

EXPERIMENTAL SECTION

Bimodal Hybrid Paste Preparation. CuMPs $1-5 \mu m$ in diameter and AgNPs 20-30 nm in diameter were purchased from Atlantic Equipment Engineers and SkySpring Nanomaterials, respectively. Glycerol (99+ %) was purchased from Alfa Aesar. Poly (vinylpolypyrrolidone) (PVP) (MW 360,000), as the binder and the most effective steric stabilizer that prevents particle agglomeration and binder, ethylene glycol (EG) (anhydrous, 99.8%), and ethyl alcohol, pure (anhydrous, ≥99.5%) were obtained from Sigma-Aldrich. All the materials were used as received. AgNPs with different conductive filler weight fractions of 2, 4, 6, 8, and 16 wt % were mixed with CuMPs. In the meantime, 0.74 g of PVP was dissolved in ethanol for 3 h under sonication at room temperature. The dissolved PVP in ethanol was mixed with 1 g of EG and 0.4 g of glycerol and sonicated for 2 h at room temperature to obtain a homogenous solution. Then, 15.4 g of CuMP/AgNP powder mixture was dispersed in the PVP solution by ultrasonication for 2 h at 120 W power and 12 kHz frequency (UP400S, Hielscher) to obtain a homogeneous dispersion of the hybrid bimodal paste (Figure 2a). The paste was then printed on a polyethylene terephthalate (PET) substrate (thickness 0.125 mm, Sigma-Aldrich) by a screen-printing mesh with rectangular patterns of length of 3 cm and width of 2 mm (MPS TF-100, Micro Printing Systems). Several factors affect the thickness of the printed trace such as screen mesh, where wider openings for the paste in the screen



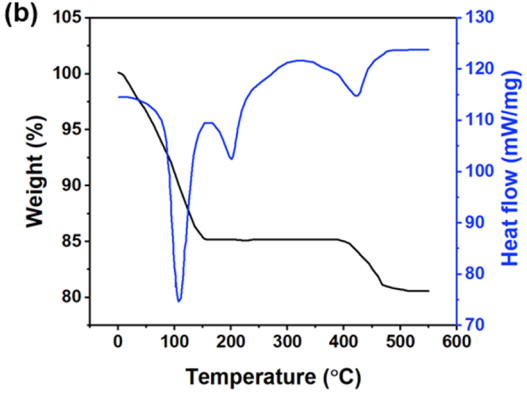


Figure 2. (a) Copper microparticle powder, silver nanoparticle powder, and the developed hybrid bimodal paste; (b) TGA and DSC thermal analysis of the developed paste.

result in higher thickness. In addition, viscosity and stencil thickness can affect the final thickness of the printed trace.

Before each printing run, the paste was mixed in a centrifugal THINKY mixer (ARE 310, THINKY) for 1 h, and after printing, the paste was dried for 30 min in an oven at 90 $^{\circ}$ C.

Photonic Sintering Process. Photonic sintering of the printed pattern was performed by IPL irradiation using a PulseForge 1200 (NovaCentrix) equipped with three xenon gas lamp drivers at room temperature and ambient conditions at a 2 cm distance from the printed trace. To obtain the minimal sheet resistance, process variables such as pulse irradiation energy density, pulse number, pulse length, and pulse offtime were optimized. For more accurate results, the pulse energy was verified with the built-in bolometer before each sintering run. We identified that for the lowest sheet resistance, a pulse length of 5 ms and an offtime of 2 s are required. To find the optimum sintering IPL settings of the printed traces, the irradiation energy was varied between 8.5 and 10.6 J/cm² with different pulse numbers (up to 6) at fixed pulse durations (5 ms). The average sheet resistance of three measurements after photonic sintering for each weight percent paste composition of CuMPs and AgNPs was recorded by using the four-probe technique (34401A, Agilent).

Material Property Characterization. Thermal analysis of the bimodal hybrid paste and PVP was performed by thermogravimetric analysis (TGA) (TG 209 F3 Tarsus, Netzsch) and differential scanning calorimetry (DSC) (214 Polyma, Netzsch) at a fixed heating rate of 18 °C/min in order to investigate the drying profile of the paste. Surface and cross-sectional morphology and elemental composition analysis of the bimodal paste were performed by an optical (Stemi 2000-c, Zeiss) and a field-emission scanning electron microscope equipped with an energy-dispersive X-ray detector (Hitachi S-4800). The through-thickness profile of the bimodal paste was investigated by confocal microscopy (Leica DCM8 Dual Core Measuring Microscope, Leica Microsystems). The packing density of the paste was analyzed by measuring percent porosity through thickness of the paste obtained from cross-sectional scanning electron microscopy images by color contrast estimation with ImageJ software.

The crystalline structure of the bimodal paste was studied by grazing incidence X-ray diffraction (GIXRD) by using a PANalytical Empyrean multipurpose diffractometer (PANalytical, Almelo, The Netherlands) with a fixed Cu K α anode (λ = 1.541, 87 Å) operating at 45 kV and 40 mA with an incident beam angle fixed at ω = 2°.

To examine oxidation resistance and electrical stability, the printed traces with different weight percent of AgNPs and optimized IPL sintering process were exposed to four environmental conditions. The stability experiments were performed in an environmental chamber with controlled relative humidity (RH) and temperature conditions set to 23 °C with 40% RH, 23 °C with 100% RH, 70 °C with 40% RH, and 70 °C with 100% RH. The changes in sheet resistance and appearance were monitored every 24 h for all samples over the course of 7 days.

Mechanical Characterization. The flexibility and adhesion of the printed traces were investigated by the standard adhesion and cyclic bending test. The adhesion test was performed according to the standard tape peeling test with Scotch tape (Scotch 898, 3M). Scotchtape peel tests were performed by sticking the sticky side of a piece of magic tape onto the printed trace and then peeling the tape off from the substrate. Qualitative Scotch-tape peel tests were performed on printed traces with different weight-percent AgNP and CuMP compositions (CuMPs-0 wt % AgNPs, CuMPs-6 wt % AgNPs, and CuMPs-16 wt % AgNPs) before and after optimized IPL sintering. To assess the long-term electromechanical stability and flexibility of the printed traces, a cyclic bending test was performed on IPL-sintered samples by a universal testing machine (eXpert4000, Admet) at a flexing rate of 10 mm/s while continuously recording changes in the electrical conductivity of the printed traces. The universal testing machine has a fixed clamp, where one end of the printed trace is fastened and the other end is clamped to a motor-driven axial displacement grip that applies the cyclic bending test to the other end of the trace. Two pieces of copper tape were pressed on the two ends of the printed trace on the substrate, followed by soldering a 2 cmlong copper wire to the copper tapes to ensure proper ohmic contact between the printed trace and electrical probes connected to the digital multimeter (34401A, Agilent). Data acquisition and storage were done by using a custom-written script in Python.

RESULTS AND DISCUSSION

Material and Electrical Property Assessment. In order to achieve high-quality sintering, the paste must be properly dried prior to the IPL sintering process. This process eliminates potential damage to the printed film by the sudden boiling and evaporation of solvents inside the deposited film during IPL irradiation.

The conductive paste is designed at a fixed metal filler percentage of 80 (with different ratios of CuMPs and AgNPs), 13% of PVP and ethanol, 5% EG as the reducing agent, and 2% glycerol; Figure 2a.

Figure 2b shows TGA and DSC analysis that were conducted to determine the proper drying process of the CuMPs-6wt % AgNP bimodal paste.

The TGA data showing an initial mass loss area from 23 to 157 °C correspond to the evaporation of the paste solvent with the majority of the solvent being evaporated at ~107 °C, as confirmed by the strong endothermic peak observed in the DSC graph. The DSC graph also shows an endothermic peak at around ~200 °C, which corresponds to the boiling temperature of EG.⁴² As the temperature increases to around 400 °C, another weight loss in the TGA data can be seen, which corresponds to the decomposition of the PVP binder (Figure S1) in the paste, as confirmed by the endothermic peak in the DSC plot. At around 460 °C, the weight loss corresponds to decomposition reaction of PVP is completed and the TGA data showed a total of 20% weight loss of the

paste, which indicates that the paste contains 80% of the conductive filler, which is in good agreement with the initial amount of the conductive filler used for paste preparation.

It should be noted that the irradiation of PVP with the photonic lamp results in a gradient decomposition through the thickness of the printed trace. While the PVP binder at the surface of the trace experiences the highest decomposition rate, the PVP at the interface undergoes less decomposition. This characteristic ensures an enhanced and effective adhesion between the substrate and the printed trace.

To avoid damage to the PET substrate with low glass transition temperature and based on the thermal analysis of the paste obtained from DSC and TGA data (Figure 2), the oven drying step for all compositions of CuMP/AgNP bimodal printed traces was set to 90 °C for 30 min. It should be noted that while higher drying temperatures of 157 °C were able to provide a faster drying time (~10 min) on more temperature-resistant substrates (e.g., glass), both drying temperatures (90 and 157 °C) resulted in the same final electrical resistance after photonic sintering with optimal settings (Figure S2). Therefore, to ensure the possibility of using the developed paste on a wider range of temperature-sensitive polymeric substrates, we utilized the lower-temperature drying procedure (90 °C for 30 min) throughout all experiments.

The sheet resistance of all printed traces with different weight percentage compositions of CuMPs and AgNPs turned out to be nonconductive after the drying process. This observation is mainly due to the presence of an insulating oxide layer (Cu_xO) around the CuMPs as a result of copper's low stability in air. In order to reduce this inherent oxide layer, a temperature of over $1000~^{\circ}\text{C}^{19}$ is needed to decompose the oxide layer. However, subjecting the trace to such high thermal energy would destroy the heat-sensitive substrate, such as PET and other organic ingredients in the paste.

One of the possible solutions to address such issue is to mix the paste with a reducing agent such as EG ($C_2H_6O_2$) and PVP that can reduce the formed Cu_xO back to copper photothermochemically at elevated temperatures. Although such temperature is higher than the glass transition temperature of PET, photonic sintering can selectively heat up the Cu_xO on the surface of the trace through absorption of the delivered photonic thermal energy without damaging the PET. Such absorption only occurs if the delivered photonic energy by the photonic lamp (200–1200 nm wavelength spectrum) to the oxide layers is higher than the band gaps of CuO and Cu_2O , which are known to be 1.2 and 2.1 eV; respectively. As soon as the photonic irradiation hits the surface of the printed trace, heated Cu_xO will react with the EG ($C_2H_6O_2$) according to the following reaction.

$$2HO(CH2)2OH + CuxO$$

$$\rightarrow 2C2H4O + CuxO$$

$$\rightarrow C4H6O2 + H2O + Cu$$

In this reaction, the delivered thermal energy induced by optical absorption of the formed $\mathrm{Cu_xO}$ results in a rise of up to the near-boiling point of EG; 160-200 °C. Accordingly, EG starts to dehydrate, forming acetaldehyde ($\mathrm{C_2H_4O}$) that reduces the $\mathrm{Cu_xO}$ to Cu through duplicative oxidation alongside diacetyl ($\mathrm{C_4H_6O_2}$) and water byproducts. ⁴² Diacetyl production during the photochemical reduction is due to duplicate oxidation of acetaldehyde, which is previously

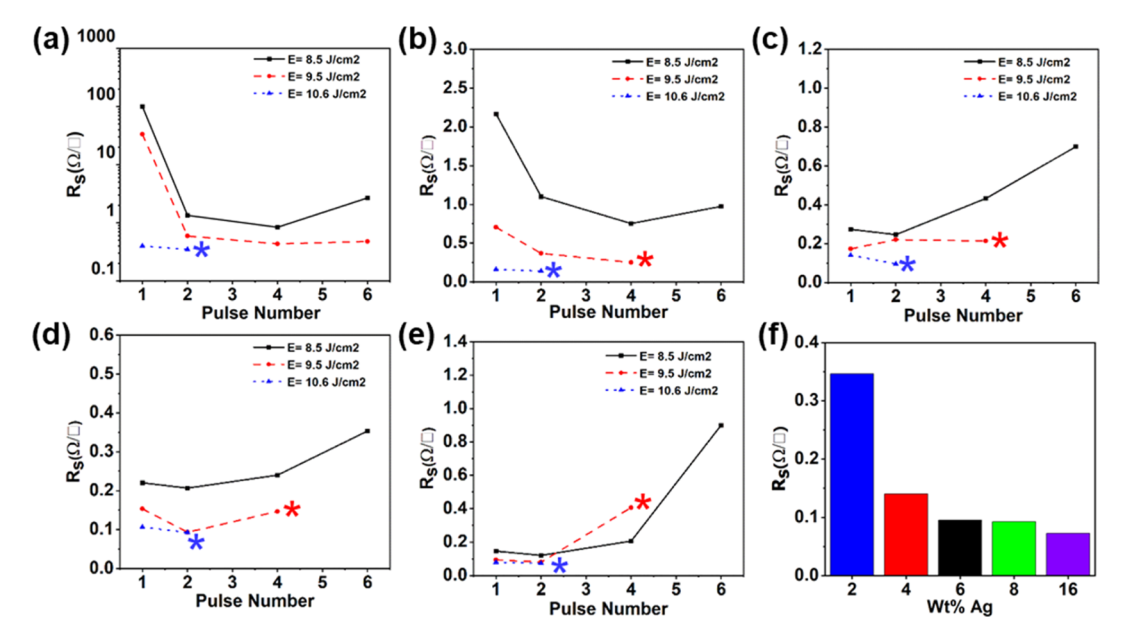


Figure 3. Sheet resistance variation of photonically sintered CuMP-AgNP hybrid bimodal printed traces at energies of 8.5, 9.5, and 10.6 J/cm² with pulse number (a) CuMPs-2 wt % AgNPs, (b) CuMPs-4 wt % AgNPs, (c) CuMPs-6 wt % AgNPs, (d) CuMPs-8 wt % AgNPs, (e) CuMPs-16 wt % AgNPs, and (f) comparison of the lowest sheet resistance obtained vs AgNP amount. Stars indicate an open circuit.

formed by EG dehydration. ⁴⁵ The results of the analysis on the developed paste with and without EG revealed that adding EG to the paste could lead the sheet resistance of the paste up to 30 times lower than before adding EG (Figure S3).

Such high photonic thermal energy also enables formation of alcohols, carboxyl acid, or acetic acid⁴⁶ through photodegradation of $PVP^{47,48}$ that could further enhance reduction of $Cu_{\nu}O.^{49,50}$

In addition, CuMPs also need to have sufficient electron pathways between one another for the transportation of electric charge. This electron pathway can be formed by adding AgNPs to the paste. As the melting temperatures of AgNPs decrease with their diameter, they require a significantly lower amount of photonic sintering energy to melt. This AgNP melting results in the formation of sufficient electron pathways between reduced CuMPs. Figure 3a-e demonstrates the resistance profile of the developed hybrid bimodal paste with the pulse number irradiated with photonic energy levels of 8.5, 9.5, and 10.6 J/cm²; respectively. Printed CuMPs-2 wt % AgNPs, CuMPs-4 wt % AgNPs, CuMPs-6 wt % AgNPs, CuMPs-8 wt % AgNPs, and CuMPs-16 wt % AgNPs could withstand up to six pulses of 8.5 J/cm² with no damage to the printed trace or substrate. The lowest achieved sheet resistance turns out to be 0.84 and 0.75 Ω/\Box for CuMPs-2 wt % AgNPs and CuMPs-4 wt % AgNPs, respectively, when exposed to four pulses of 8.5 J/cm². However, as the number of pulses increases beyond four for these two compositions, the resistance starts to increase, indicating reoxidation of Cu microparticles. On the other hand, the lowest sheet resistance observed for CuMPs-6 wt % AgNPs, CuMPs-8 wt % AgNPs, and CuMPs-16 wt % AgNPs once exposed to 8.5 J/cm² of energy is 0.24, 0.20, and 0.12 Ω/\Box , respectively, only after two pulses prior to Cu reoxidation initiation, which can be observed in the increased peak intensity associated with the Cu₂O in the GIXRD spectrum of the bimodal paste for both CuMPs-6 wt % AgNP and CuMPs-16 wt % AgNP compositions (Figure S4a) compared to optimum photonic sintering setting crystalline structures. However, this is not the

case when a higher energy (10.6 J/cm²) is delivered to the trace as the surface of the trace starts to develop localized cracks and defects caused by overheating and thermally deforming the PET polymeric substrate (Figure S4b,c). This is mainly because as the amount of AgNPs in the paste is increased, they absorb a higher portion of the light, which results in transferring a higher amount of thermal energy to the adjacent CuMPs, therefore expediting the reoxidation of the CuMPs.

Upon increasing the amount of photonic energy to 9.5 J/ cm², an interesting phenomenon starts to happen, in which except for CuMPs-2 wt % AgNPs, all the other compositions start to burn under light upon increasing the pulse number beyond 4. In addition, although the decreasing trend of the sheet resistance with an increasing pulse number is observed for bimodal paste compositions of up to CuMPs-6 wt % AgNPs, reoxidation of the printed pattern is observed for higher compositions, that is, CuMPs-8 wt % AgNPs and CuMPs-16 wt % AgNPs. For 9.5 J/cm² of pulse energy, the optimum sheet resistance measured for CuMPs-2 wt % AgNPs, CuMPs-4 wt % AgNPs, CuMPs-6 wt % AgNPs, CuMPs-8 wt % AgNPs, and CuMPs-16 wt % AgNPs is 0.43, 0.25, 0.21, 0.09, and 0.081 Ω/\Box , respectively. It is obvious that a higher AgNP amount in the paste leads to lower sheet resistance. The lowest sheet resistance achieved throughout the entire series of experiments for every single composition is once the printed trace is irradiated with only two pulses of 10.6 J/cm² energy and can be summarized as 0.34, 0.14, 0.095, 0.092, and 0.072 Ω/\square for CuMPs-2 wt % AgNPs, CuMPs-4 wt % AgNPs, CuMPs-6 wt % AgNPs, CuMPs-8 wt % AgNPs, and CuMPs-16 wt % AgNPs, respectively (Figure 3f).

It should be mentioned that for an energy level up to 10.6 J/cm^2 , the CuMPs-0 wt % AgNPs paste composition showed no conductivity after photonic sintering (Figure S5a); however, as the energy rises to 13.34 J/cm^2 , the trace shows low-level conductivity ($\sim G\Omega/\square$) with local cracks at the edges of the trace (Figure S5b). Upon further increase in the energy density to 16.3 J/cm^2 , although a minimum sheet resistance of $590 \Omega/$

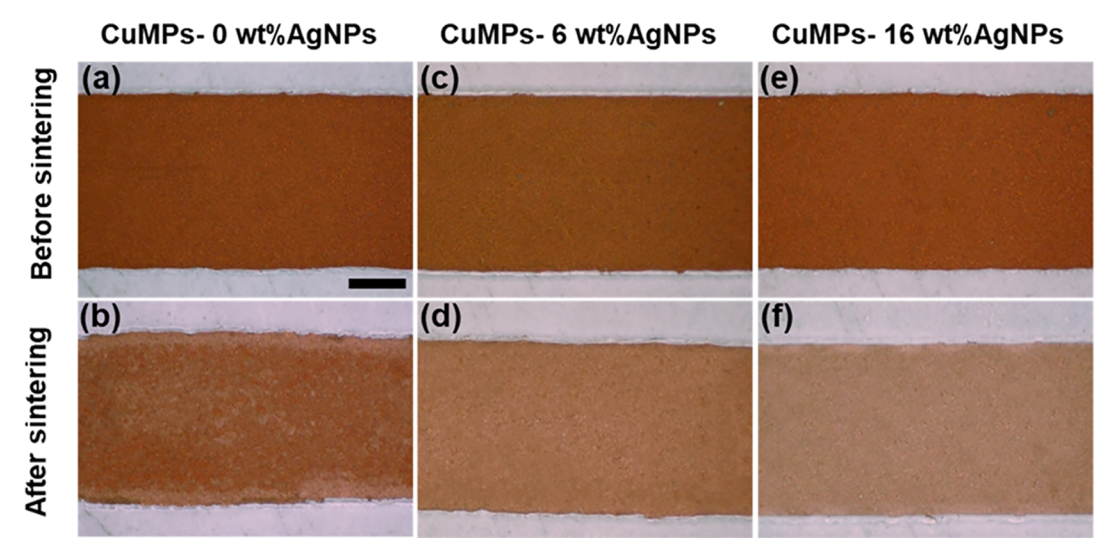


Figure 4. Surface microscopic pictures of printed traces before (a,c,e) and after (b,d,f) photonic sintering with optimized process settings from left to right for CuMPs-0wt % AgNPs, CuMPs-6wt % AgNPs, and Cu-16 wt % Ag bimodal pastes, respectively (scale bar: 1 mm).

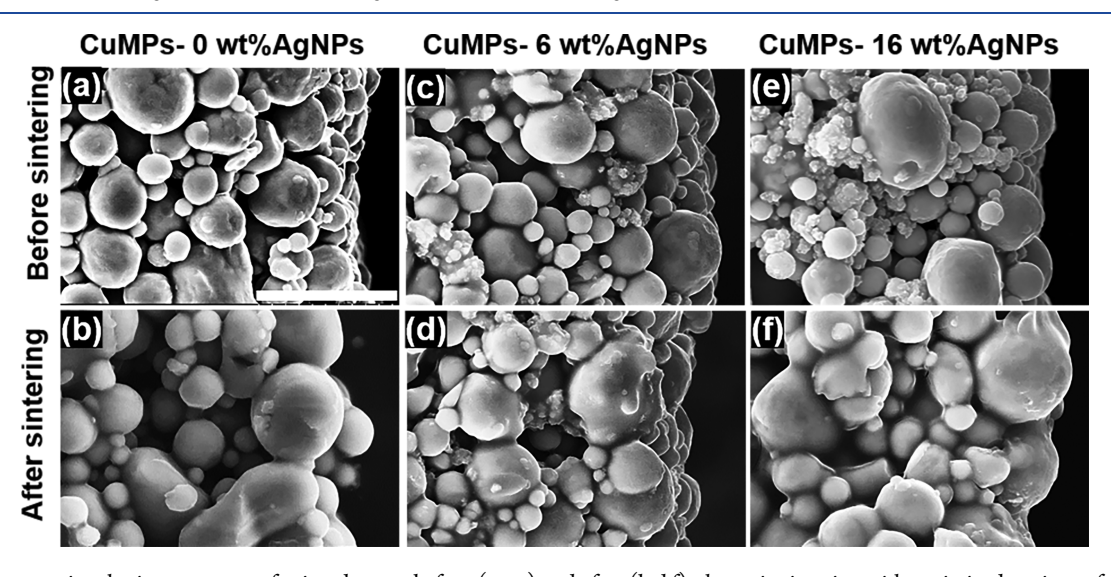


Figure 5. Cross-sectional microstructure of printed traces before (a,c,e) and after (b,d,f) photonic sintering with optimized settings of two pulses at 10.6 J/cm^2 energy from left to right for CuMPs-0wt % AgNPs, CuMPs-6wt % AgNPs, and CuMPs-16wt % AgNPs, respectively (scale bar: $10 \mu m$).

is obtained, the surface micrograph of the trace reveals large defected areas as well as paste evaporation (Figure S5c).

Figure 3f reveals that the addition of only 6 wt % AgNPs to the hybrid bimodal paste can turn a nonconductive trace to a highly conductive one with a sheet resistance of as low as 0.095 Ω/\square ($\rho\sim190~\mu\Omega\cdot$ cm) after photonic sintering. Moreover, this value for sheet resistance reaches a plateau once the composition of AgNPs increases by 2 wt %. Although a significant decrease in sheet resistance of the trace is observed for CuMPs-16 wt % AgNPs (0.072 Ω/\square) that results in the highest achieved volume resistance of $\sim145~\mu\Omega\cdot$ cm, adding this much of AgNPs to the paste is not recommended as this results in a relatively high final cost of the printed trace. On the other hand, compared to CuMPs-16 wt % composition, the CuMPs-6 wt % AgNP composition results in both close level of conductivity and significantly lower final cost that makes it the top candidate for the developed bimodal paste.

Figure 4a—f compares the surface optical micrographs of CuMPs-0 wt % AgNPs, CuMPs-6 wt % AgNPs, and CuMPs-16 wt % AgNPs printed traces before and after photonic sintering

with two pulses of 10.6 J/cm² energy density. It can be seen that no significant color change is visible for the CuMPs-0 wt % AgNP printed trace after photonic sintering (Figure 4a,b). Nevertheless, the higher the AgNP content in the hybrid bimodal paste, the brighter the surface of the printed trace after photonic sintering (Figure 4c-f). This observation provides a criterion for a qualitative assessment tool for the sheet resistance of the developed hybrid bimodal paste, where the brighter surfaces after photonic sintering show a higher conductivity level compared to the darker ones. This phenomenon is mostly attributed to the fact that the addition of AgNPs to the paste not only acts as a nanowelders between CuMPs, but also prevents reoxidation of Cu after photonic sintering and exposure to oxygen. This is mainly because high photonic thermal energy promotes the formation of a network of AgNPs along Cu grain boundaries that hinders reoxidation of CuMPs.⁵¹ To further evaluate the sheet resistance achieved with the developed bimodal hybrid paste, we looked at microstructural evolution of the printed trace along the thickness with the composition of CuMPs-0 wt % AgNPs,

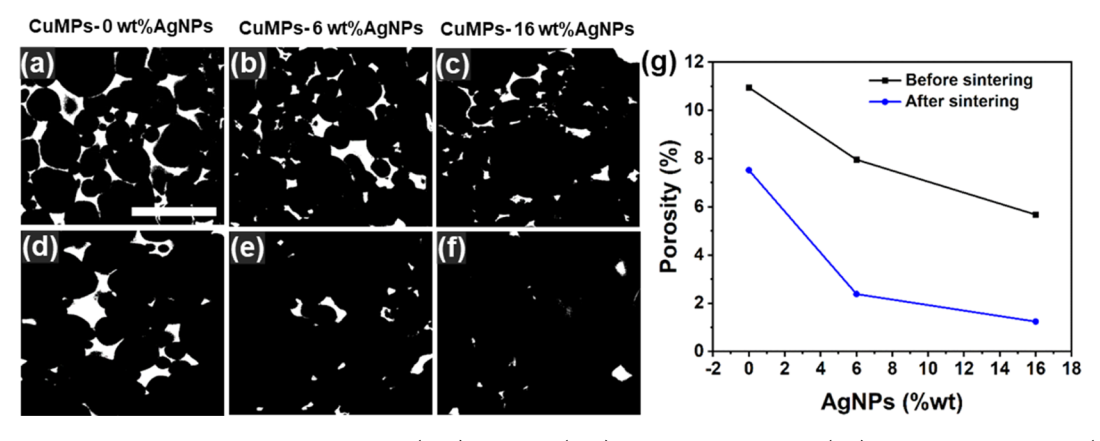


Figure 6. Packing density analysis of printed traces before (a-c) and after (d-f) photonic sintering for (a,d) CuMPs-0 wt % AgNP, (b,e) CuMPs-6 wt % AgNP, and (c,f) CuMPs-16 wt % AgNP printed trace; (g) comparison of porosity of the printed traces before and after photonic sintering with different wt % of AgNPs (scale bar: $10 \mu m$).

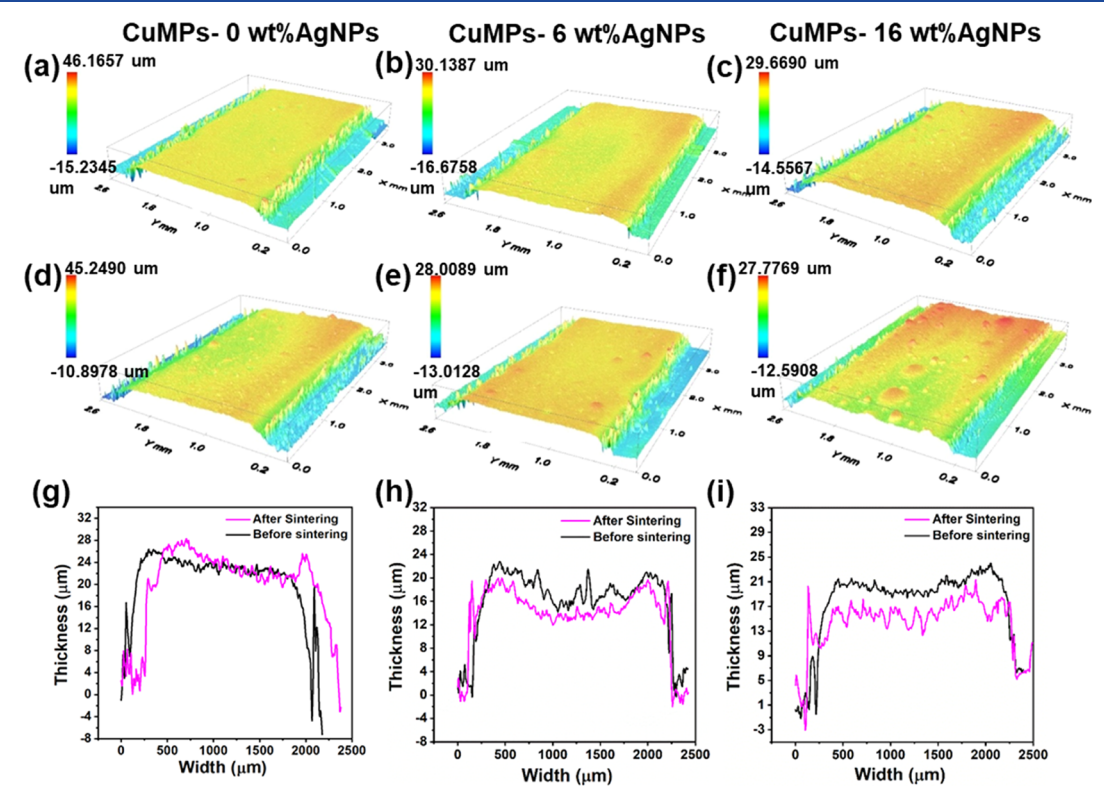


Figure 7. 3D confocal microscopy of printed traces (a-c) before and (d-f) after photonic sintering for (a,d) CuMPs-0 wt % AgNPs, (b,e) CuMPs-6 wt % AgNPs, and (c,f) CuMPs-16 wt % AgNPs; (g-i) thickness profiles of printed traces before and after photonic sintering: (g) CuMPs-0 wt % AgNPs, (h) CuMPs-6 wt % AgNPs, and (i) CuMPs-16 wt % AgNPs.

CuMPs-6 wt % AgNPs, and CuMPs-16 wt % AgNPs before and after photonic sintering by two pulses of 10.6 J/cm² energy density (Figure 5a-f). The CuMPs-0 wt % AgNP composition does not show regions of particles fusing together after photonic sintering (Figure 5b), which explains why this composition is nonconductive after irradiation with the pulsed light.

Upon increasing the content of AgNPs in the bimodal hybrid paste, localized sites of particles fused together, thus forming electron pathways with the adjacent CuMPs (Figure 5d,f). During sintering, photonic energy is selectively absorbed by AgNPs in the paste and due to their high surface area, they heat up and melt within milliseconds. This phenomenon results in atomic diffusion and necking growth-induced surface

melting, ^{28,52,53} resulting in overall fewer pores in the printed trace that contributes to enhanced conductivity as well. This diffusion is further confirmed from the EDX data on the CuMPs-16 wt % AgNP composition, in which the fusion layer with elemental compotion of at 82.48 atomic% of Ag and only at 0.48 atomic% of Cu (Figure S6C) is detected, whereas these numbers at a nonfusion layer are 76.13 atomic% for Cu and 14.11 atomic% for Ag (Figure S6b).

Pores in the printed trace can be one of the main contributing factors that result in inefficient sintering and high resistivity. In some cases, when the pores are trapped within the microstructure of the trace, it might be cumbersome to identify them and understand how they can influence the sintering quality only by cross-sectional micrographs. One

possible solution is packing density analysis by ImageJ software,e where color-contrast images of the printed traces before and after sintering can visually provide evidence on the quantitative porosity reduction. Figure 6 demonstrates ImageJ packing density analysis of CuMPs-0 wt % AgNPs, CuMPs-6 wt % AgNPs, and CuMPs-16 wt % AgNPs before (Figure 6a—c) and after photonic sintering (Figure 6d—f) by two pulses of 10.6 J/cm² energy density. These results demonstrate that increasing the amount of AgNPs in the paste results in improved packing density for CuMPs-0 wt % AgNPs, CuMPs-6 wt % AgNPs, and CuMPs-16 wt % AgNPs to 7.5, 2.3, and 1.2%; respectively, after photonic sintering (Figure 6g).

Another quantitative approach that accounts for porosity estimation through the thickness of the printed traces is to look at the thickness profile of the trace before and after photonic sintering. Figure 7 illustrates the 3D microscopy profile of the printed traces with compositions of CuMPs-0 wt % AgNPs, CuMPs-6 wt % AgNPs, and CuMPs-16 wt % AgNPs before (Figure 7a-c) and after (Figure 7d-f) photonic sintering by two pulses of 10.6 J/cm² energy density. For all compositions, before sintering, a thickness of $\sim 20 \, \mu \text{m}$ was measured. Although there is almost no thickness reduction for CuMPs-0 wt % AgNPs (Figure 7g), there is a thickness reduction of average of 4 and 6 μ m for CuMPs-6wt % AgNP (Figure 7h) and CuMPs-16wt % AgNP (Figure 7i) compositions, respectively, which results from decreased porosity and binder removal due to flash irradiation, which is mostly promoted by AgNP melting. Further increase in the amount of AgNPs in the paste (20 wt %) not only does not result in a significant thickness reduction after photonic sintering (Figure S7a) but also could result in more risk of particle aggregation, significant surface damage, and formation of nodule-like structures after photonic sintering (Figure S7c).

The formed aggregated sites due to higher content of AgNPs in the paste might result in ineffective sintering by forming nodule-like structures due to nonuniform distribution of the nanoparticles throughout the CuMP network (Figures 5e and 7f). However, this effect is minimal for optimum CuMPs-6 wt % AgNP concentration, as can be observed in Figures 5d and 7e.

The crystalline structure of sintered hybrid bimodal paste with different compositions of CuMPs and AgNPs is shown in Figure 8. Although a large oxide peak is still visible for the CuMPs-0 wt % AgNP composition, as the amount of AgNPs

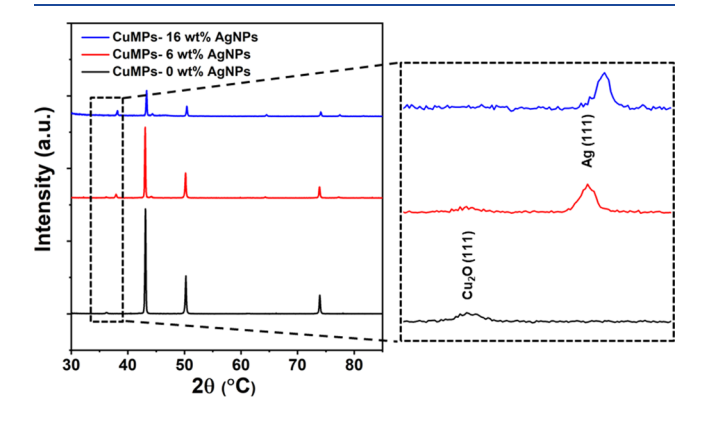


Figure 8. GIXRD spectrum of the hybrid bimodal paste after photonic sintering with two pulses at $10.6~\mathrm{J/cm^2}$ energy for CuMPs-0wt % AgNP, CuMPs-6wt % AgNP, and CuMPs-16wt % AgNP compositions.

increases, the intensity of the peak decreases up to a point where the oxide peak disappears for the CuMPs-16 wt % AgNP composition, indicating the complete reduction of Cu₂O. This indicates that to get a highly sintered trace with high metallic purity, a combination of EG-reducing mechanism and formation of a network of AgNPs along Cu grain boundaries is required. This corresponds to the obtained sheet resistance of 0.095 and 0.072 Ω/\Box for sintered CuMPs-6 wt % AgNPs and CuMPs-16 wt % AgNP compositions, respectively, which only can be achieved by complete removal of the oxide layer formed around the copper particles. This removal allows AgNPs to efficiently act as a nanowelder between CuMPs and turn the printed trace into a highly conductive pattern.

Sheet Resistance Stability Assessment. Reoxidation of copper after sintering upon exposure to air mostly nucleates from the particle grain boundaries; 51 however, we believe that dissolving a network of AgNPs along Cu grain boundaries at photonic sintering-induced high thermal energy can significantly delay Cu reoxidation and maintain low sheet resistance even in humid environments. Figure 9a-d is an experimental proof of this claim, where we show sheet resistance evolution of CuMPs-2 wt % AgNP, CuMPs-4 wt % AgNP, CuMPs-6 wt % AgNP, CuMPs-8 wt % AgNP, and CuMPs-16 wt % AgNP hybrid bimodal paste photonically sintered by the optimized setting of two pulses at 10.6 J/cm² energy density for 1 week. Figure 9a shows the changes in the metal films under ambient conditions (T = 23 °C and RH = 40%). The sheet resistance of CuMPs-2 wt % AgNP hybrid bimodal paste undergoes an abrupt increase to 4.43 Ω/\Box after 3 days, while other compositions of CuMP/AgNP bimodal paste with higher AgNP amounts remain at a stable level. This result is consistent with the surface morphology inspection analysis of the CuMPs-2 wt % AgNP and CuMPs-16 wt % AgNP bimodal compositions after 7 days of exposure to an ambient environment where dark regions can be seen over the surface of CuMPs-2 wt % AgNPs, indicating reoxidation of the printed trace, while CuMPs-16 wt % AgNPs show no sign of reoxidation by changing color (Figure 9e,f). As the temperature of the environment is increased to 70 °C, the onset of sheet resistance abrupt change for CuMPs-2 wt % AgNPs starts from day 2 of the measurements that goes up to 20.18 Ω/\Box at the end of day 7 (Figure 9b). In addition to CuMPs-2 wt % AgNP composition, CuMPs-4 wt % AgMPs show unstable sheet resistance values after 5 days of exposure to 70 °C, rising to 1.97 Ω/\square at the end of day 7. On the other hand, for higher amounts of AgNPs, that is, 6, 8, and 16 wt %, Figure 9b indicates stable sheet resistance during the 7 days of measurements. This finding is consistent with the sheet resistance evolution results obtained when the RH is set to 100% and temperature is varied between the minimum and maximum values of 23 and 70 °C (Figure 9c,d). However, the differences arise from the cases where AgNP content in the bimodal paste is less than 6 wt %. For instance, compared to the room-temperature environment where the sheet resistance of CuMPs-4 wt % AgNP bimodal paste remains stable throughout the experiment, as the RH rises to 100%, a significant increase in the sheet resistance from 0.14 to 76.6 Ω / at the end of day 7 can be seen (Figure 9c). This trend is even more severe once the printed pattern is placed in an environment with T = 70 °C and RH = 100%, where CuMPs-2 wt % AgNP and CuMPs-4 wt % AgNP bimodal compositions become nonconductive only after 3 and 5 days of exposure to the environment, respectively (Figure 9d). In contrast,

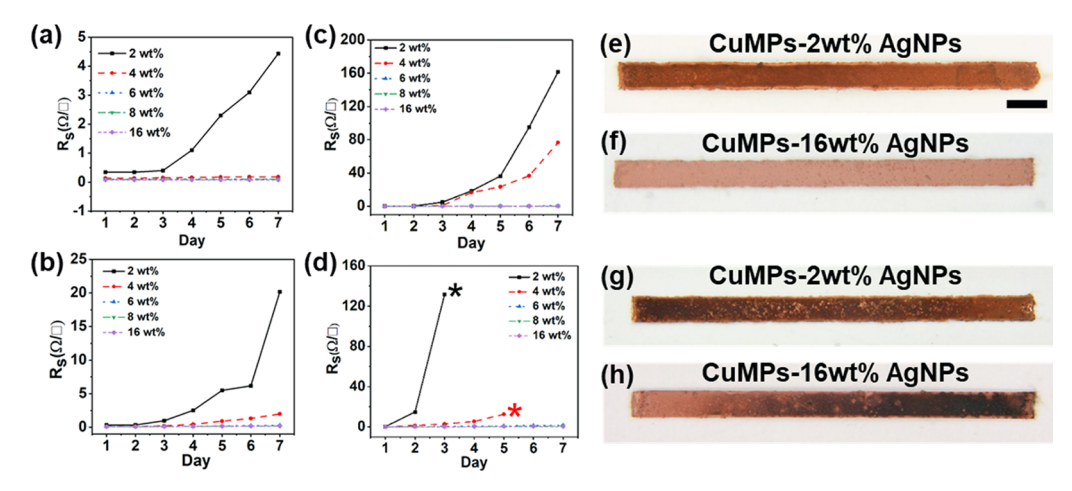


Figure 9. Oxidation sheet resistance evolution of printed traces after photonic sintering with two pulses at 10.6 J/cm² energy subject to (a) ambient conditions (23 °C and 40% RH), (b) room temperature with elevated humidity (23 °C and 100% RH), (c) high temperature (70 °C) and 40% RH, and (d) high temperature (70 °C) and 100% RH, photographs of the printed traces after 7 days in (e,f) room temperature with elevated humidity (23 °C and 100% RH), and (g–h) high temperature (70 °C) and 100% RH. Stars indicate an open circuit (scale bar: 3 mm).

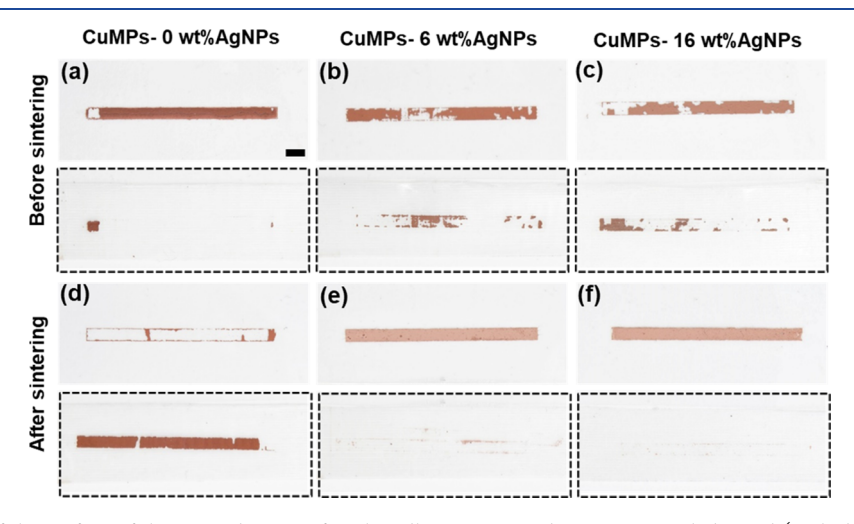


Figure 10. Photographs of the surface of the printed traces after the adhesion test and respective peeled taped (with dotted border) (a-c) before and (d-f) after photonic sintering with the optimized photonic setting of two pulses at 10.6 J/cm^2 energy from left to right for CuMPs-0wt % AgNPs, CuMPs-6wt % AgNPs, and CuMPs-16wt % AgNPs; respectively (scale bar: 3 mm).

CuMPs-6 wt % AgNP, CuMPs-8 wt % AgNP, and CuMPs-16 wt % AgNP compositions remain stable over the period of 7 days of measurements (Figure 9c,d). Comparing the photographs of CuMPs-2 wt % AgNPs and CuMPs-16 wt % AgNPs after 7 days of exposure to T = 70 °C and RH = 100% reveals the fact that large areas of surface defects and bubbles on the surface of CuMPs-2 wt % AgNPs obstructs the electron pathway formation by AgNPs after photonic sintering (Figure 9g), while no deep defect on the surface of the CuMPs-16 wt % AgNPs is observed (Figure 9h). It can be concluded that oxidation stability of the bimodal paste heavily depends on the amount of AgNPs in the paste, where the addition of 6 wt % of AgNPs should be sufficient to avoid reoxidation of the printed trace after photonic sintering. This is mainly because as the amount of AgNPs is increased in the bimodal paste, the number of Ag-rich phases on the surface of the printed trace increases, thus showing a higher tendency to avoid reoxidation of the surface due to lower surface energy of Ag (1.25 J/m²) compared to Cu (1.85 J/cm²).^{28,54}

Flexibility and Adhesion Assessment. Figure 10a-f demonstrates results of the adhesion test for CuMPs-0 wt %

AgNP, CuMPs-6 wt % AgNP, and CuMPs-16 wt % AgNP hybrid bimodal paste (from left to right) with the peeled tape before (Figure 10a-c) and after (Figure 10d-f) photonic sintering with optimum settings. The results indicate firm and enhanced adhesion of the printed trace to PET, where both CuMPs-6 wt % AgNP and CuMPs-16 wt % AgNP printed traces do not detach from the substrate after photonic sintering. We believe that this is mainly because of the improved packing density of the printed trace after photonic sintering. The addition of AgNPs significantly contributes to improving the packing density of the paste by minimizing the pores within the Cu microstructure of the printed trace. It should be noted that minimal pore density within the material results in less likelihood of crack initiation and growth as the pore sites in the printed trace can act as strong stress concentrates and contribute to accelerating the crack growth. Herein, we identified that the addition of only 6 wt % AgNPs to the CuMPs can significantly improve the packing density of the material and avoid crack nucleation within the material for the highest adhesion performance. The results of the cyclic bending test on different compositions of hybrid bimodal paste

photonically sintered with the optimum setting reveal an interesting point that CuMPs-2 wt % AgNP bimodal paste can only withstand less than 70 cycles before electrical disconnection. On the other hand, CuMPs-4 wt % AgNPs although maintain their conductivity until the end of the 200th cycle of bending, they show an increase in sheet resistance to $107.82 \ \Omega/\Box$ (Figure 11c). Comparatively, a higher amount of

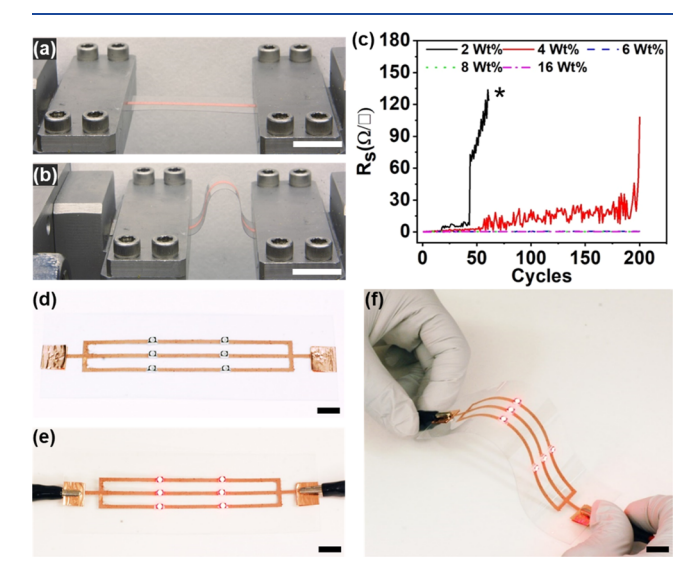


Figure 11. Photonically sintered CuMPs-6wt % AgNP printed trace (a) before and (b) after subjecting to cyclic bending (c) sheet resistance change of the printed traces with various weight percentages of AgNPs form 0 to 16 wt % (e) as a function bending cycles, a 3×2 array of circuit lighting with photonically sintered CuMPs-6 wt % AgNP printed trace (d) before and (e,f) after applying DC voltage to the circuit. Star indicates high resistance and an open circuit (all scale bars: 1 cm).

AgNPs in the bimodal paste results in relatively stable sheet resistance even after 200 bending cycles (Figure 11c). This high mechanical and electrical stability of the CuMPs/AgNP hybrid bimodal paste is attributed to the improved densification of the microstructure induced by enhanced packing density created by the AgNP welding joints created between the CuMP network. Figure 11d,e demonstrates a simple circuit application of 3×2 arrays of light-emitting diodes (LEDs) bonded to the surface of the screen-printed CuMPs-6 wt % AgNP hybrid bimodal paste by fast-drying silver paint and photonically sintered by the optimal setting. The flexible printed circuit can withstand mechanical bending with a high radius of curvature with no change in the illumination intensity of the LEDs (Figure 11f).

Printed Wireless Humidity Sensor. A highly stable and conductive paste provides the unique possibility of printing low-cost RF elements such as antennas and coils, where high electrical conductivity is critical for their effective performance. To demonstrate an application of the developed bimodal conductive paste in printed low-cost RF technologies, an all-printed chipless sensor is designed and characterized for wireless moisture monitoring inside packaged products. Increased moisture levels in packaging can result in decreased product quality, low shelf life, and bacterial growth, leading to food-borne illness. Figure 12a—d shows the process of printing a wireless sensor and assembly inside a commercial cardboard box to monitor the moisture content of sealed packages. The simplicity of the process enables the sensors to

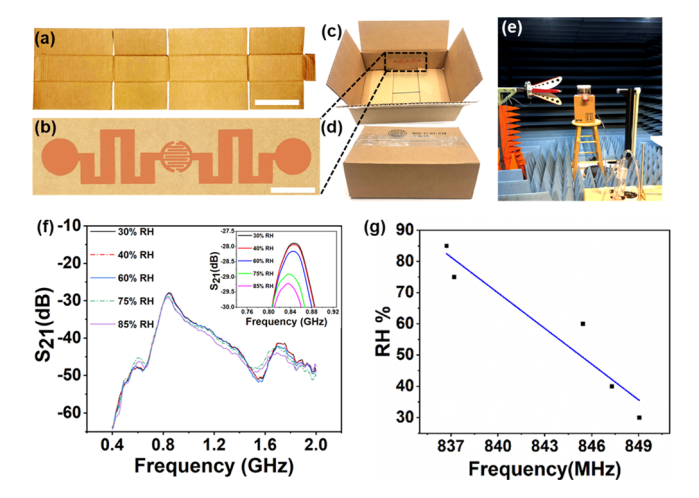


Figure 12. Photograph of the cardboard substrate (a) before and (b) after direct printing of the photonically sintered CuMPs-6wt % AgNP sensor, (c,d) a commercial cardboard package box with the printed wireless moisture sensor inside the (e) moisture measurement experimental setup in the anechoic chamber, (f) measured S_{21} as a function of frequency for RH levels of 30-85% and demonstration of the resonant frequency shift with increased RH in the environment (inset), and (g) measured resonant frequency variation of the printed sensor over the 30-85% RH range. (scale bar: 2 mm).

be printed directly into the interior of the packaging box and potentially be used in the standard packaging process of products. The device consists of an interdigitated electrode (IDE) structure as a capacitive moisture sensor that bridges the two meandered extensions of a dipole antenna. The wireless moisture sensing involves a reader sending an interrogation signal to the printed sensor. When the sensor receives the interrogation signal, it retransmits part of the incident signal back to the reader by embedding the resonant frequency information in the reflected RF spectrum. The resonant frequency of the retransmitted signal is a function of the effective length of the antenna and the dielectric properties of the medium surrounding the IDE structure, as described in the equation below.

$$f_{\rm r} = \frac{c}{2L\sqrt{\varepsilon_{\rm eff}}}$$

where L is the length of the antenna, $\varepsilon_{\rm eff}$ is the effective dielectric constant of the surrounding substrate, and c is the speed of light. Alteration of the dielectric properties of the cardboard substrate, due to the absorption of moisture at elevated humidity levels, changes the net capacitance of the IDE section of the sensor, which, in turn, leads to a shift in the resonant frequency of the sensor. This change in the resonant frequency can be detected wirelessly in the reflected signal as a resonant peak in the RF spectrum received by the external reader antenna.

The strength of the retransmitted signal depends on the conductivity of the metal used in the sensor pattern. The high conductivity of the metallic pattern is an important requirement to improve the quality of the RF signal retransmission from the sensor to the reader antenna. On the other hand, the final cost of the material and scalability of the process is critical for the sensors to be economically feasible and practical to be implemented in the packaging process.

To meet the cost requirement, the conductive traces for the wireless sensor was prepared by using stencil printing a

bimodal paste with a minimum amount of AgNPs (CuMPs-6 wt % AgNPs) and optimized photonic sintering settings, which provided the needed stable electrical and mechanical performance. The printed passive chipless wireless moisture sensor with an overall dimension of 10 cm is shown in Figure 12b.

The wireless moisture monitoring performance of the sensor was tested in an anechoic chamber within an experimental setup that allowed changing the RH level around the wireless sensor using a gas bubbler containing water at a constant temperature (21 °C). A cross-polarized horn antenna was used as a reader antenna to detect the changes in the resonant frequency of the sensor under different RH levels; Figure 12e. The shift in the resonant frequency of the sensor was obtained by analyzing the backscattered signal from the sensor tag, which is received by the horn antenna that is connected to a Vector Network Analyzer (E5072A, Agilent Technologies).

The performance and sensitivity of the printed sensor are evaluated within the RH range of 30–85%. Figure 12f shows the backscattered signal spectrum from the sensor where S_{21} is measured by the horn antenna over a frequency range of 0.4–2 GHz. The results demonstrate a shift in the resonant frequency (f_r) from ~849 MHz for 30% RH to 836.72 MHz for 85% RH (Figure 12f inset) with a linear sensitivity of -3.08 %RH/MHz ($r^2 \sim 91\%$) (Figure 12g).

As demonstrated, the described wireless sensor exploits the hygroscopic characteristics of the cardboard substrate as the sensing element for detecting changes in RH within the environment. The random distributed cellulolytic microstructure network of the cardboard provides a natural hygroscopic dielectric material for sensing humidity. At elevated RH conditions, the water molecules in the ambient environment are absorbed within the cellulose fibers in the cardboard. Due to the high dielectric constant value (\sim 80), the absorbed moisture in the cardboard leads to an increase in its effective dielectric constant. This change results in an overall increase in the capacitive IDE element of the sensor and is reflected as a decrease in the overall resonant frequency of the wireless sensor.

CONCLUSIONS

We have demonstrated a novel formulation of a bimodal CuMP and AgNP paste with photonic sintering for printing highly conductive circuits on temperature-sensitive polymeric substrates. The photonic irradiation energy not only induced AgNP melting that results in providing sufficient electron pathway between Cu microparticles but also could reduce Cu_xO to bulk copper photothermochemically. The minimum sheet resistance observed was 0.072 Ω/\Box for CuMPs-16 wt % AgNPs after sintering with two pulses at 10.6 J/cm² energy with superior oxidation resistance stability of up to 7 days at 70 °C and 100% RH environment. Scanning electron microscopy and GIXRD analysis confirmed AgNP melting and electron pathway formation between CuMPs as well as reduction of Cu₂O after photonic sintering, justifying the exceptionally high level of the conductivity measured. The printed hybrid bimodal paste showed promising adhesion and electromechanical properties with only 6 wt % addition of AgNPs with high cyclic bending stability. Finally, we demonstrated an application of the developed bimodal paste for screen-printing a wireless passive moisture sensor that allows for in situ quality monitoring of moisture-sensitive content in a sealed modified atmosphere package in atmosphereic condition. Our sensor

can easily be integrated into the current packing process for tracking and quality monitoring of food and pharmaceuticals.

ASSOCIATED CONTENT

Supporting Information

The Supporting Information is available free of charge at https://pubs.acs.org/doi/10.1021/acsaelm.1c00345.

Thermal behavior of PVP, effect of drying temperature and duration on sheet resistance of the oven-dried CuMPs-6 wt % AgNP printed trace, followed by photonic sintering with optimum setting of two pulses at 10.6 J/cm² energy, effect of EG on sheet resistance of the paste with CuMPs-6 wt % AgNP and CuMPs-16 wt % AgNP compositions, reoxidation, and damage assessment of the hybrid bimodal paste after photonic sintering with excessive thermal energy, effect of increasing thermal energy on sheet resistance of CuMPs-0 wt % AgNP printed trace EDX spectrum and elemental composition analysis (at %) of the photonically sintered CuMPs-16 wt % AgNP printed trace with optimum settings, and 3D confocal microscopy analysis of CuMPs-20 wt % AgNP printed trace (PDF)

AUTHOR INFORMATION

Corresponding Author

Rahim Rahimi — School of Materials Engineering, Purdue University, West Lafayette, Indiana 47907, United States; Birck Nanotechnology Center, Purdue University, West Lafayette, Indiana 47907, United States; orcid.org/0000-0001-5302-782X; Email: rrahimi@purdue.edu

Authors

Amin Zareei — School of Materials Engineering, Purdue University, West Lafayette, Indiana 47907, United States; Birck Nanotechnology Center, Purdue University, West Lafayette, Indiana 47907, United States; Occid.org/0000-0002-6176-5475

Sarath Gopalakrishnan – Birck Nanotechnology Center and School of Electrical and Computer Engineering, Purdue University, West Lafayette, Indiana 47907, United States

Zeynep Mutlu — School of Materials Engineering, Purdue University, West Lafayette, Indiana 47907, United States; Birck Nanotechnology Center, Purdue University, West Lafayette, Indiana 47907, United States

Zihao He — School of Electrical and Computer Engineering, Purdue University, West Lafayette, Indiana 47907, United States

Samuel Peana — Birck Nanotechnology Center and School of Electrical and Computer Engineering, Purdue University, West Lafayette, Indiana 47907, United States

Haiyan Wang — School of Materials Engineering, Purdue University, West Lafayette, Indiana 47907, United States; School of Electrical and Computer Engineering, Purdue University, West Lafayette, Indiana 47907, United States; orcid.org/0000-0002-7397-1209

Complete contact information is available at: https://pubs.acs.org/10.1021/acsaelm.1c00345

Notes

The authors declare no competing financial interest.

ACKNOWLEDGMENTS

The authors thank the staff of the Birck Nanotechnology Center at Purdue University for their technical support. The authors also thank David Berels, Dr. Babak Arfaei, and Prof. Miko Cakmak for insightful discussion. Funding for this project was provided by the Ford Motor Company and the School of Materials Engineering at Purdue University. Z.H. and H.W. acknowledge the support from the U.S. National Science Foundation (DMR-1809520) for the XRD effort.

REFERENCES

- (1) Berggren, M.; Nilsson, D.; Robinson, N. D. Organic Materials for Printed Electronics. *Nat. Mater.* **2007**, *6*, 3–5.
- (2) Perelaer, J.; Smith, P. J.; Mager, D.; Soltman, D.; Volkman, S. K.; Subramanian, V.; Korvink, J. G.; Schubert, U. S. Printed Electronics: The Challenges Involved in Printing Devices, Interconnects, and Contacts Based on Inorganic Materials. *J. Mater. Chem.* **2010**, 20, 8446–8453.
- (3) Kamyshny, A.; Magdassi, S. Conductive Nanomaterials for 2D and 3D Printed Flexible Electronics. *Chem. Soc. Rev.* **2019**, 48, 1712–1740.
- (4) Kamyshny, A.; Magdassi, S. Conductive Nanomaterials for Printed Electronics. *Small* **2014**, *10*, 3515–3535.
- (5) Huang, Q.; Zhu, Y. Printing Conductive Nanomaterials for Flexible and Stretchable Electronics: A Review of Materials, Processes, and Applications. *Adv. Mater. Technol.* **2019**, *4*, 1970029.
- (6) Chopra, S.; Pham, A.; Gaillard, J.; Parker, A.; Rao, A. M. Carbon-Nanotube-Based Resonant-Circuit Sensor for Ammonia. *Appl. Phys. Lett.* **2002**, *80*, 4632–4634.
- (7) Habas, S. E.; Platt, H. A. S.; Van Hest, M. F. A. M.; Ginley, D. S. Low-Cost Inorganic Solar Cells: From Ink to Printed Device. *Chem. Rev.* **2010**, *110*, 6571–6594.
- (8) Ong, K. G.; Zeng, K.; Grimes, C. A. A Wireless, Passive Carbon Nanotube-Based Gas Sensor. *IEEE Sens. J.* **2002**, *2*, 82–88.
- (9) Chang, J. S.; Facchetti, A. F.; Reuss, R. A Circuits and Systems Perspective of Organic/Printed Electronics: Review, Challenges, and Contemporary and Emerging Design Approaches. *IEEE J. Emerg. Sel. Top. Circuits Syst.* **2017**, *7*, 7–26.
- (10) Sridhar, A.; Blaudeck, T.; Baumann, R. R.; Enas, N. S. Inkjet Printing as a Key Enabling Technology for Printed Electronics. *Mater. Matters* **2011**, *6*, 12–15.
- (11) Liang, J.; Tong, K.; Pei, Q. A Water-Based Silver-Nanowire Screen-Print Ink for the Fabrication of Stretchable Conductors and Wearable Thin-Film Transistors. *Adv. Mater.* **2016**, *28*, 5986–5996.
- (12) Wang, J.; Yan, C.; Chee, K. J.; Lee, P. S. Highly Stretchable and Self-Deformable Alternating Current Electroluminescent Devices. *Adv. Mater.* **2015**, *27*, 2876–2882.
- (13) Wu, W. Inorganic Nanomaterials for Printed Electronics: A Review. *Nanoscale* **2017**, *9*, 7342–7372.
- (14) Jiang, Z.; Fukuda, K.; Xu, X.; Park, S.; Inoue, D.; Jin, H.; Saito, M.; Osaka, I.; Takimiya, K.; Someya, T. Reverse-Offset Printed Ultrathin Ag Mesh for Robust Conformal Transparent Electrodes for High-Performance Organic Photovoltaics. *Adv. Mater.* **2018**, *30*, 1870190.
- (15) Rong, Y.; Hou, X.; Hu, Y.; Mei, A.; Liu, L.; Wang, P.; Han, H. Synergy of Ammonium Chloride and Moisture on Perovskite Crystallization for Efficient Printable Mesoscopic Solar Cells. *Nat. Commun.* **2017**, *8*, 14555.
- (16) Wünscher, S.; Abbel, R.; Perelaer, J.; Schubert, U. S. Progress of Alternative Sintering Approaches of Inkjet-Printed Metal Inks and Their Application for Manufacturing of Flexible Electronic Devices. *J. Mater. Chem. C* **2014**, *2*, 10232–10261.
- (17) Ghosh, S. Electroless Copper Deposition: A Critical Review. *Thin Solid Films* **2019**, *669*, 641–658.
- (18) Li, W.; Sun, Q.; Li, L.; Jiu, J.; Liu, X.-Y.; Kanehara, M.; Minari, T.; Suganuma, K. The Rise of Conductive Copper Inks: Challenges and Perspectives. *Appl. Mater. Today* **2020**, *18*, 100451.

- (19) Zhang, J.; Wayne Richardson, H. Copper Compounds. LLMANN'S Encyclopedia of Industrial Chemistry; Wiley, 2006; pp 91–119
- (20) Niittynen, J.; Sowade, E.; Kang, H.; Baumann, R. R.; Mäntysalo, M. Comparison of Laser and Intense Pulsed Light Sintering (IPL) for Inkjet-Printed Copper Nanoparticle Layers. *Sci. Rep.* **2015**, *5*, 8832.
- (21) Oh, G.-H.; Hwang, H.-J.; Kim, H.-S. Effect of Copper Oxide Shell Thickness on Flash Light Sintering of Copper Nanoparticle Ink. *RSC Adv.* **2017**, *7*, 17724–17731.
- (22) Hwang, H.-J.; Chung, W.; Kim, H. In Situ Monitoring of Flash-Light Sintering of Copper Nanoparticle Ink for Printed Electronics. *Nanotechnology* **2012**, *23*, 485205.
- (23) Kang, J. S.; Kim, H. S.; Ryu, J.; Thomas Hahn, H.; Jang, S.; Joung, J. W. Inkjet Printed Electronics Using Copper Nanoparticle Ink. J. Mater. Sci. Mater. Electron. 2010, 21, 1213–1220.
- (24) Park, S.-H.; Chung, W.-H.; Kim, H.-S. Temperature Changes of Copper Nanoparticle Ink during Flash Light Sintering. *J. Mater. Process. Technol.* **2014**, *214*, 2730–2738.
- (25) Gaikwad, A. M.; Steingart, D. A.; Nga Ng, T.; Schwartz, D.; Whiting, G. A Flexible High Potential Printed Battery for Powering Printed Electronics. *Appl. Phys. Lett.* **2013**, *102*, 233302.
- (26) Rager, M. S.; Aytug, T.; Veith, G. M.; Joshi, P. Low-Thermal-Budget Photonic Processing of Highly Conductive Cu Interconnects Based on CuO Nanoinks: Potential for Flexible Printed Electronics. ACS Appl. Mater. Interfaces 2016, 8, 2441–2448.
- (27) Paglia, F.; Vak, D.; van Embden, J.; Chesman, A. S. R.; Martucci, A.; Jasieniak, J. J.; Della Gaspera, E.; Manufacturing, C.; Avenue, B. Photonic Sintering of Copper through the Controlled Reduction of Printed CuO Nanocrystals. *ACS Appl. Mater. Interfaces* **2015**, *7*, 25473–25478.
- (28) Li, W.; Hu, D.; Li, L.; Li, C.-F.; Jiu, J.; Chen, C.; Ishina, T.; Sugahara, T.; Suganuma, K. Printable and Flexible Copper-Silver Alloy Electrodes with High Conductivity and Ultrahigh Oxidation Resistance. ACS Appl. Mater. Interfaces 2017, 9, 24711–24721.
- (29) Chaudhuri, R. G.; Paria, S. Core/Shell Nanoparticles: Classes, Properties, Synthesis Mechanisms, Characterization, and Applications. *Chem. Rev.* **2012**, *112*, 2373–2433.
- (30) Zhu, G.; Lin, Z. H.; Jing, Q.; Bai, P.; Pan, C.; Yang, Y.; Zhou, Y.; Wang, Z. L. Toward Large-Scale Energy Harvesting by a Nanoparticle-Enhanced Triboelectric Nanogenerator. *Nano Lett.* **2013**, *13*, 847.
- (31) Lee, C.; Kim, N. R.; Koo, J.; Lee, Y. J.; Lee, H. M. Cu-Ag Core-Shell Nanoparticles with Enhanced Oxidation Stability for Printed Electronics. *Nanotechnology* **2015**, *26*, 455601.
- (32) Grouchko, M.; Kamyshny, A.; Magdassi, S. Formation of Air-Stable Copper-Silver Core-Shell Nanoparticles for Inkjet Printing. *J. Mater. Chem.* **2009**, *19*, 3057–3062.
- (33) Tam, S. K.; Ka, T.; Fung, Y.; Ming, K. Copper Pastes Using Bimodal Particles for Flexible Printed Electronics. *J. Mater. Sci.* **2016**, *51*, 1914–1922.
- (34) Gao, Y.; Zhang, H.; Li, W.; Jiu, J.; Nagao, S.; Sugahara, T.; Suganuma, K. Die Bonding Performance Using Bimodal Cu Particle Paste Under Different Sintering Atmospheres. *J. Electron. Mater.* **2017**, 46, 4575–4581.
- (35) Dai, Y. Y.; Ng, M.; Anantha, P.; Lin, D.; Li, Z.; Gan, C.; Tan, C. Enhanced Copper Micro/Nano-Particle Mixed Paste Sintered at Low Temperature for 3D Interconnects. *Appl. Phys. Lett.* **2016**, *108*, 263103.
- (36) Kanzaki, M.; Kawaguchi, Y.; Kawasaki, H. Fabrication of Conductive Copper Films on Flexible Polymer Substrates by Low-Temperature Sintering of Composite Cu Ink in Air. ACS Appl. Mater. Interfaces 2017, 9, 20852.
- (37) Joo, S.; Hwang, H.; Kim, H. Highly Conductive Copper Nano/ Microparticles Ink via Fl aAsh Light Sintering for Printed Electronics. *Nanotechnology* **2014**, *25*, 265601.
- (38) Yu, M.-H.; Joo, S.; Kim, H. Multi-Pulse Flash Light Sintering of Bimodal Cu Nanoparticle-Ink for Highly Conductive Printed Cu Electrodes. *Nanotechnology* **2017**, *28*, 205205.

- (39) Rosen, Y. S.; Yakushenko, A.; Offenhäusser, A.; Magdassi, S. Self-Reducing Copper Precursor Inks and Photonic Additive Yield Conductive Patterns under Intense Pulsed Light. *ACS Omega* **2017**, *2*, 573–581.
- (40) Gao, Y.; Li, W.; Zhang, H.; Jiu, J.; Hu, D.; Suganuma, K. Size Controllable Synthesis of Bimodal Cu Particles by Polyol Method and Their Application in Die Bonding for Power Devices. *IEEE Trans. Compon. Packag. Manuf. Technol.* **2018**, *8*, 2190–2197.
- (41) Hwang, H.; Joo, S.; Kim, H. Copper Nanoparticle/Multiwalled Carbon Nanotube Composite Films with High Electrical Conductivity and Fatigue Resistance Fabricated via Flash Light Sintering. ACS Appl. Mater. Interfaces 2015, 7, 25413–25423.
- (42) Han, S.; Hong, S.; Yeo, J.; Kim, D.; Kang, B.; Yang, M.-Y.; Ko, S. H. Nanorecycling: Monolithic Integration of Copper and Copper Oxide Nanowire Network Electrode through Selective Reversible Photothermochemical Reduction. *Adv. Mater.* 2015, 27, 6397–6403.
- (43) Rafea, M. A.; Roushdy, N. Determination of the Optical Band Gap for Amorphous and Nanocrystalline Copper Oxide Thin Films Prepared by SILAR. *J. Phys. D: Appl. Phys.* **2008**, *42*, 015413.
- (44) Kang, B.; Han, S.; Kim, J.; Ko, S.; Yang, M. One-Step Fabrication of Copper Electrode by Laser-Induced Direct Local Reduction and Agglomeration of Copper Oxide Nanoparticle. *J. Phys. Chem. C* **2011**, *115*, 23664–23670.
- (45) Mizoshiri, M.; Tanokuchi, A. Direct Writing of Cu-Based Micropatterns inside Cu 2 O Nanosphere Films Using Green Femtosecond Laser Reductive Sintering. *Opt. Mater. Express* **2020**, *10*, 2533–2541.
- (46) Hwang, H.-J.; Oh, K.; Kim, H. All-Photonic Drying and Sintering Process via Flash White Light Combined with Deep-UV and near- Infrared Irradiation for Highly Conductive Copper Nano-Ink. *Sci. Rep.* **2016**, *6*, 19696.
- (47) Horikoshi, S.; Hidaka, H.; Serpone, N. Photocatalyzed Degradation of Polymers in Aqueous Semiconductor Suspensions: V. Photomineralization of Lactam Ring-Pendant Polyvinylpyrrolidone at Titania/Water Interfaces. *J. Photochem. Photobiol., A* **2001**, *138*, 69–77.
- (48) Kaczmarek, H.; Kaminska, A.; Swiatek, M.; Rabek, J. Photo-Oxidative Degradation of Some Water-Soluble Polymers in the Presence of Accelerating Agents. *Die Angewandte Makromolekulare Chemie* 1998, 261–262, 109–121.
- (49) Soininen, P. J.; Elers, K.-E.; Saanila, V.; Kaipio, S.; Sajavaara, T.; Haukka, S. Reduction of Copper Oxide Film to Elemental Copper. *J. Electrochem. Soc.* **2005**, *152*, G122.
- (50) Yeh, M.-S.; Yang, Y.-S.; Lee, Y.-P.; Lee, H.-F.; Yeh, Y.-H.; Yeh, C.-S. Formation and Characteristics of Cu Colloids from CuO Powder by Laser Irradiation in 2-Propanol. *J. Phys. Chem. B* **1999**, 103, 6851–6857.
- (51) Li, J.; Li, Y.; Wang, Z.; Bian, H.; Hou, Y.; Wang, F. Ultrahigh Oxidation Resistance and High Electrical Conductivity in Copper-Silver Powder. *Sci. Rep.* **2016**, *6*, 39650.
- (52) Xu, S.; Tian, M.; Wang, J.; Xu, J.; Redwing, J. M.; Chan, M. H. W. Nanometer-Scale Modification and Welding of Silicon and Metallic Nanowires with a High-Intensity Electron Beam. *Small* **2005**, *1*, 1221–1229.
- (53) Cui, Q.; Gao, F.; Mukherjee, S.; Gu, Z. Joining and Interconnect Formation of Nanowires and Carbon Nanotubes for Nanoelectronics and Nanosystems. *Small* **2009**, *5*, 1246–1257.
- (54) Malviya, K. D.; Chattopadhyay, K. Temperature- and Size-Dependent Compositionally Tuned Microstructural Landscape for Ag-46 Atom % Cu Nanoalloy Prepared by Laser Ablation in Liquid. *J. Phys. Chem. C* **2016**, *120*, 27699–27706.
- (55) Kuswandi, B.; Wicaksono, Y.; Jayus, M.; Abdullah, A.; Heng, L. Y.; Ahmad, M. Smart Packaging: Sensors for Monitoring of Food Quality and Safety. Sens. Instrum. Food Qual. Saf. 2011, 5, 137–146. (56) Biji, K. B.; Ravishankar, C. N.; Mohan, C. O. Smart Packaging Systems for Food Applications: A Review. J. Food Sci. Technol. 2015, 52, 6125–6135.

■ NOTE ADDED AFTER ASAP PUBLICATION

This paper was originally published ASAP on August 13, 2021. Due to a production error, an incorrect graphic was placed for Figure 5. The corrected version was reposted on August 15, 2021.